

Curved Magnetism in CrI₃

Alexander Edström,^{1,2} Danila Amoroso,³ Silvia Picozzi,³ Paolo Barone,⁴ and Massimiliano Stengel^{1,5}

¹*Institut de Ciència de Materials de Barcelona (ICMAB-CSIC), Campus UAB, 08193 Bellaterra, Spain*

²*Department of Applied Physics, School of Engineering Sciences,*

KTH Royal Institute of Technology, AlbaNova University Center, 10691 Stockholm, Sweden

³*Consiglio Nazionale delle Ricerche CNR-SPIN, c/o Università degli Studi 'G. D'Annunzio', 66100, Chieti, Italy*

⁴*Consiglio Nazionale delle Ricerche CNR-SPIN, Area della Ricerca di Tor Vergata,*

Via del Fosso del Cavaliere 100, I-00133 Rome, Italy

⁵*ICREA - Institució Catalana de Recerca i Estudis Avançats, 08010 Barcelona, Spain*

Curved magnets attract considerable interest for their unusually rich phase diagram, often encompassing exotic (e.g., topological or chiral) spin states. Micromagnetic simulations are playing a central role in the theoretical understanding of such phenomena; their predictive power, however, rests on the availability of reliable model parameters to describe a given material or nanostructure. Here we demonstrate, by focusing on monolayer CrI₃, how non-collinear-spin polarized density-functional theory can be used to determine the flexomagnetic coupling coefficients in real systems. In particular, we find a crossover as a function of curvature between a magnetization normal to the surface to a cycloidal state, which we rationalize in terms of effective anisotropy and Dzyaloshinskii–Moriya contributions to the magnetic energy. Our results reveal an unexpectedly large impact of spin-orbit interactions on the curvature-induced anisotropy, which we discuss in the context of the existing phenomenological models.

Introduction - Inhomogeneous deformations in the form of local curvature are ubiquitous at the nanoscale, and are currently regarded as a rich playground for new phenomena. [1–3] Understanding their effects is crucial for the materials design of tailored functionalities, e.g., in flexible electronics, as well as for the tunability of the existing ones via external mechanical stimuli [4, 5]. A notable example is flexoelectricity [1], i.e. the emergence of a macroscopic electric polarization in presence of a non-uniform strain, highly attractive as a potential piezoelectric replacement [5] or in the emerging field of strain-enabled photovoltaics [6]. Atomically thin two-dimensional (2D) crystals and membranes, due to their extreme flexibility and their natural tendency towards rippling [7], appear as the ideal class of materials to explore these effects.

Strain gradients can have a comparably strong impact on magnetism [2, 3, 8], via a curvature-induced modification of the spin coupling parameters that is commonly referred to as *flexomagnetism* [9]. Representative examples include the emergence of curvature-induced Rashba spin-orbit interaction [10–12], asymmetric magnon dispersions [13], topological magnetism [14], magnetic anisotropies and effective Dzyaloshinskii–Moriya interactions (DMI) [2, 14–16]. Remarkably, the geometric DMI can drive the formation of chiral and topological spin configurations even in absence of SOC [2], thus lifting the traditional requirement of heavy elements in the crystal structure for exotic magnetic orders to occur. A very exciting development in this context is the recent experimental report of strain-gradient-induced DMI resulting in a room-temperature Skyrmion lattice [17]. Thanks to impressive advances in experimental fabrication and characterization techniques, [18, 19] additional observations of these effects in the lab are anticipated in the near

future. From the point of view of theory, it would be desirable to support the experimental efforts by developing a quantitatively accurate understanding of flexomagnetism in real materials. Several simplifying assumptions are currently adopted in micromagnetic simulations of curved nanostructures (see, e.g., Ref. [2] and references therein), which potentially limit their predictive power. For example, the effective DMI and anisotropy in the curved structure are modeled as non-relativistic effects via a coordinate transformation operated on the isotropic exchange interaction. While appearing reasonable, such an approximation has not been tested in a realistic context, and its validity is still an open question.

Ab initio electronic-structure methods have been playing a leading role in understanding low-dimensional magnets and formulating new predictions [20–23]. Their application to flexomagnetism is, however, still at an infancy stage and challenging in the framework of density-functional theory (DFT): curvature breaks translational symmetry, thwarting at first sight the applicability of the Bloch theorem and plane-wave basis sets, which the vast majority of code implementations rely on, thus requiring large periodic supercells that may easily contain many hundreds of atoms. The recent discovery of long-range magnetic order in monolayers of CrI₃ and other Van der Waals compounds [24–27] provides a natural playground to study curvature-induced effects on magnetic properties from first principles. In addition to their practical [28] and fundamental [22, 29, 30] interest, two-dimensional magnets with only few atoms per surface unit allow for the simulation of bent geometries to be tractable (even if expensive) within DFT [31]. Nonetheless, the few existing studies have limited the computational burden by targeting collinear spin structures [31–33]. This is clearly insufficient for understanding the emergence of nontriv-

ial magnetic states in a bent layer, which requires a fully non-collinear treatment of the spins in presence of curvature.

Here, we use non-collinear-spin DFT to investigate the magnetic properties of CrI_3 as a function of an externally applied curvature. The latter is incorporated by focusing on nanotube (NT) geometries with radii (R) between 7.5 Å and 30 Å. By comparing the energies of different magnetic states as a function of R , we show that curvature leads to a crossover between an out-of-plane magnetization for the flat monolayer (corresponding to a radial magnetization for large- R NTs), to a cycloidal state at larger curvatures (smaller R), which is stabilized by an effective curvature-induced DMI [16]. To rationalize this finding, we construct a continuum model, whose parameters are fully determined from first principles, in terms of the spin stiffness, anisotropy and DMI strength and their dependence on curvature. We find that SOC has a surprisingly strong impact on the curvature-induced effective anisotropy, which qualitatively departs from the assumptions of earlier phenomenological models.

Methods - Calculations are performed using the projector augmented wave (PAW) [34, 35] method, as implemented in VASP [36–38]. The local density approximation (LDA) is used for the exchange-correlation together with an additional Coulomb repulsion [39] of $U = 0.5$ eV on Cr d-states. The cutoff energy for the plane-waves basis set is 350 eV. The value of U and other computational settings are chosen in accordance with Ref. [21]. A $4 \times 4 \times 1$ k -point mesh is used for calculations on the freestanding monolayer [40] of CrI_3 , while $1 \times 1 \times 4$ k -points are used for the NTs, with a Gaussian smearing of 50 meV. A vacuum of 15 Å is inserted between the monolayers or nanotubes. The NT structures are optimized by means of damped molecular dynamics using standard collinear calculations with a ferromagnetic spin ordering until forces are smaller than 3 meV/Å, or less for smaller NTs. Specifically, we consider (N, N) arm-chair nanotubes [41] for $N = 4, 5, 6, 7, 8, 10, 12, 16$, as illustrated in Fig. 1. This means that N units of the cell marked with a red rectangle in Fig. 1(a) are wrapped around the circumference of the NT. The Cr-Cr distance is $d = 3.87$ Å, whereby the NT radii are approximately NR_0 with $R_0 = \frac{3d}{2\pi} = 1.85$ Å. Energy calculations on different magnetic states were performed via constrained non-collinear magnetic calculations, with and without SOC, using a penalty energy for spins deviating from the desired configuration [42, 43]. We carefully tested that the results are independent of the penalty energy for a wide range of curvatures [44].

Results - Energy differences of the relaxed NTs with collinear ferromagnetism, relative to the flat monolayer, are reported as a function of the curvature $\kappa = 1/R$ in Fig. 1(b). The calculated data show a smooth monotonic behavior with κ , confirming the accuracy of the structural relaxations. The fitted bending modulus, $\alpha =$

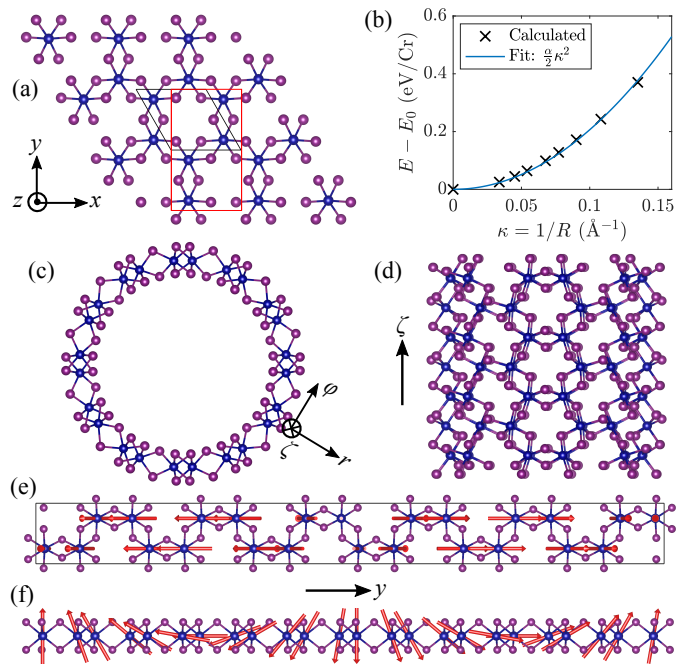


Figure 1. (a) Monolayer CrI_3 (Cr - blue, I -purple) with black lines showing the primitive 8 atom unit cell (2 Cr and 6 I) while the red lines show the doubled unit cell, N of which are used to construct (N, N) nanotubes. (b) Calculated energy (per Cr) as a function of curvature. (c) $N = 6$ nanotube from above and (d) side. (e) Supercell strip for a spin spiral with wavelength equal to the circumference of the $N = 6$ nanotube, seen from above and (f) side, with arrows showing the magnetic moments of the spin spiral considered, with $\mathbf{m}_i = [0, -\sin(qy_i), \cos(qy_i)]$.

2.2 eV, falls in the same range as other monolayers of transition metal dichalcogenides [45]. This elastic contribution, of order 1 eV per Cr atom, dominates by far the energetics of bending. The dependence on the magnetic ordering is typically three orders of magnitude smaller (~ 1 meV/Cr), as we shall see in the following while discussing our results with non-collinear spins and SOC.

In Fig. 2, we show the energies of the three main spin states that we focus on in this work. They are magnetized either along the azimuthal direction $\hat{\phi}$ (E_ϕ), the radial direction \hat{r} (E_r), or with all spins parallel to a direction perpendicular to $\hat{\zeta}$ (E_\perp). All energies are relative to the axial state with spins aligned along the $\hat{\zeta}$ -axis of the NT, which we consider as our energy zero at any given R henceforth. In the limit of large R we recover the known ground state of the flat monolayer, which is ferromagnetic with out-of-plane (OP) magnetization. Such state is stabilized by an effective magnetic anisotropy constant, $\mathcal{K}_0 = E_{\text{IP}} - E_{\text{OP}} = 0.75$ meV, which we define and calculate as the energy difference between in-plane (IP) and OP magnetization in the flat monolayer. (Note that \mathcal{K}_0 , in addition to the effects of single-ion anisotropy, also accounts for anisotropic symmetric ex-

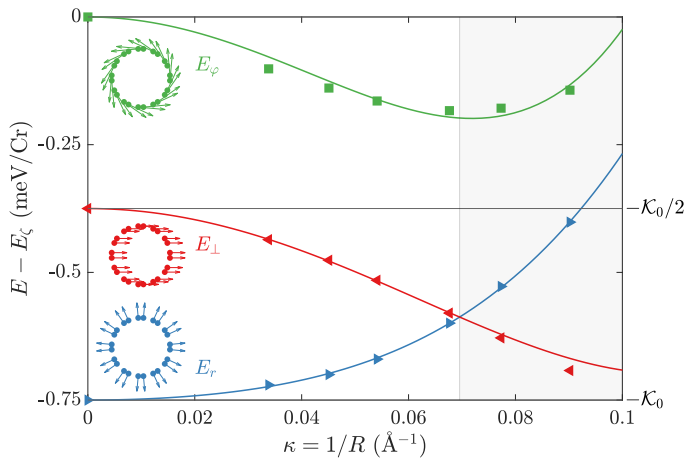


Figure 2. Energies E_{\perp} , E_{φ} and E_r , relative to E_{ζ} , as functions of curvature κ , for the different states schematically represented in the insets, with magnetization along $\hat{\mathbf{e}}_{\perp} \perp \hat{\zeta}$, $\hat{\varphi}$ and \hat{r} , respectively. Solid lines show energies from the continuum model discussed in the text.

change, whose importance in CrI_3 was recently pointed out. [21]) In the same limit, E_{φ} tends to zero, as the azimuthal state becomes degenerate with the axial one, while E_r approaches $-\mathcal{K}_0$. The energy of the perpendicular state, E_{\perp} , tends to $-\mathcal{K}_0/2$ for reasons that we shall clarify shortly. At smaller R , E_{φ} undergoes a slight decrease and then increases again, overall remaining higher in energy than the other two spin states. Meanwhile, E_r displays a monotonous increase with curvature, as the angle between neighbouring spins (and hence the exchange energy) increases. Interestingly, the magnetic state with parallel spins, normal to the NT axis, shows a decreasing energy E_{\perp} , eventually leading to a crossover between the two spin configurations at $\kappa \approx 0.07 \text{ \AA}^{-1}$, where $E_r = E_{\perp}$. At larger curvatures ($\kappa > 0.07 \text{ \AA}^{-1}$), $E_r > E_{\perp}$, with the latter state becoming the lowest in energy among those considered here.

The possibility for curvature to profoundly affect magnetism, even leading to new chiral or topological magnetic structures, has been pointed out before [2, 9]. The magnetic crossover shown in Fig. 2 is indeed reminiscent of those discussed in Ref. [16], for opposite sign of \mathcal{K}_0 . To facilitate the discussion of our results in the context of existing continuum models, we project our magnetic configurations onto a cylindrical (locally orthogonal) coordinate system [see Fig. 1(c)], where (ζ, φ) span the tangential plane of the nanotube surface, and r is normal to it. Within the (ζ, φ, r) system, the “radial” and “azimuthal” magnetization states correspond to constant values of either m_r or m_{φ} , while the “perpendicular” state (the ground state at large curvatures) shows a periodic out-of-phase modulation of m_r and m_{φ} along the tube circumference. More precisely, the latter state acquires the mathematical form of a spin cycloid, where

$\mathbf{m}_i = [0, -\sin(qy_i), \cos(qy_i)]$ and the propagation vector is $q = 1/R$; an illustration is provided in Fig. 1(e)-(f). The equal mixture of azimuthal and radial spin components in the perpendicular state explains why E_{\perp} tends to $-\mathcal{K}_0/2$ in the large-radius limit. Remarkably this also means, based on the results of Fig. 2, that curvature leads to a transition to a cycloidal magnetic ground state in the curvilinear frame of the bent surface.

In order to understand the origin of such a behavior, we consider the following continuum energy density,

$$\varepsilon = A [\partial_{\varphi} m_{\alpha}]^2 + \mathcal{K}_{\varphi} m_{\varphi}^2 + \mathcal{K}_r m_r^2 + \mathcal{D} [m_r \partial_{\varphi} m_{\varphi} - m_{\varphi} \partial_{\varphi} m_r], \quad (1)$$

where A , \mathcal{K}_i and \mathcal{D} are the spin stiffness, anisotropy and DMI parameters, $\partial_{\varphi} = \frac{1}{R} \frac{\partial}{\partial \varphi}$ and $m_{\alpha} = m_{\alpha}(\varphi)$ is one of the three curvilinear components of the magnetization density. (We consider m_{α} as a constant function of the axial ζ coordinate.) Note that all parameters in Eq. (1) depend on curvature, e.g. $A = A(\kappa = \frac{1}{R})$. To extract this dependence from our DFT calculations we fit Eq. 1, at each R , to the calculated energies of the three magnetic states in Fig. 2. The azimuthal and radial anisotropy constants are trivially provided by two of the three sets of data shown therein: $\mathcal{K}_{\varphi} = E_{\varphi}$ and $\mathcal{K}_r = E_r$. Separating the remaining two terms (spin stiffness and effective DMI) is computationally more involved, since their contributions to the energy of the perpendicular state, $E_{\perp} = A\kappa^2 - \mathcal{D}\kappa + \frac{1}{2}(\mathcal{K}_r + \mathcal{K}_{\varphi})$, are linearly dependent. (Note that, by symmetry, A and $\mathcal{D}\kappa$ are both even functions of κ .) In order to extract also $A(\kappa)$ and $\mathcal{D}(\kappa)$, we additionally perform calculations for cycloidal states of the form $\mathbf{m} = \cos(n\varphi)\hat{r} - \sin(n\varphi)\hat{\varphi}$, with integer values $n > 1$, consistent with 2π -periodicity in φ . ($n = 0$ and $n = 1$ correspond to the radial and perpendicular magnetization states, already described). This procedure allows us to uniquely resolve $A(\kappa)$, $\mathcal{D}(\kappa)$ and $\mathcal{K}(\kappa)$ at the discrete set of curvatures considered in our first-principles calculations. For practical purposes, we then interpolate these data with appropriate low-order polynomials of κ (details in the SI [44]), which yields the continuous curves plotted in Fig. 2.

The resulting separate energy contributions $A\kappa^2$, $\mathcal{D}\kappa$ and \mathcal{K}_{α} from the effective spin stiffness, DMI and anisotropy parameters are plotted as functions of curvature in Fig. 3(a). This decomposition allows us to clarify the physical origin of the cycloidal ground state obtained at larger κ . The increase in the spin stiffness energy with curvature leads to an increase in the energy cost of the spin cycloids, relative to a FM state. A non-zero \mathcal{D} (linear in κ), however, also develops with curvature, which together with the changes in the anisotropy energies, eventually favors the stabilization of the $n = 1$ cycloidal state. Note that the largest contribution to the energy comes precisely from the DMI term. At $\kappa \approx 0.1 \text{ \AA}^{-1}$, $\mathcal{D}\kappa \approx 1 \text{ meV/Cr}$. Thus, the value of \mathcal{D}

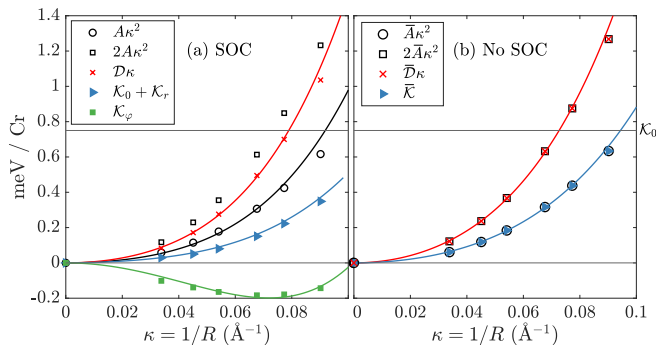


Figure 3. Energy contributions $A\kappa^2$, $\mathcal{D}\kappa$ and \mathcal{K} , from the effective exchange, DMI and anisotropy terms, with SOC in (a) and without SOC in (b).

reaches almost 1 meV/Å, similar as the interfacial DMI of a surface of Fe on W [20, 46]. For the flat, centrosymmetric CrI₃ monolayer, the DMI arises as an interaction term between second neighbours, and it was estimated to be around 60 μeV or even smaller [47, 48], whereas electric field (\mathcal{E}) induced DMI between nearest Cr-neighbours was reported to be 14 μeV for $\mathcal{E}_z \simeq 1.55$ V/nm [47]; both values are orders of magnitude smaller than the effective, curvature-induced DMI energy found here.

Earlier phenomenological studies [2, 14–16] showed the appearance of effective anisotropy and DMI terms in curvilinear 1D and 2D magnets, consistent with our findings. Remarkably, such effects were predicted even in absence of SOC, i.e., within the assumption of isotropic exchange interactions. To check whether such assumptions are reliable in our case, in the following we benchmark the model of Ref. [16], which we have adapted to our specific geometry (details in the SI [44]), against our first-principles results. We find, consistent with the conclusions of Sheka *et al.* [16], that in absence of SOC the coefficients of Eq. 1 are no longer independent, but enjoy the following mutual relationships [44],

$$\overline{\mathcal{D}} = 2\overline{A}\kappa, \quad \overline{\mathcal{K}} = \overline{\mathcal{K}}_r = \overline{\mathcal{K}}_\varphi = \overline{A}\kappa^2. \quad (2)$$

(We use an overline symbol to indicate quantities defined and calculated without SOC.) Our results of Fig. 3(a) manifestly violate such conditions: neither the effective anisotropies nor the DMI appear to be related to the spin stiffness energy in any obvious way. To clarify the role of SOC in this unexpected behavior, we have repeated all our first-principles calculations without SOC, and followed the exact same post-processing procedure to extract \overline{A} , $\overline{\mathcal{D}}$ and $\overline{\mathcal{K}}$ as functions of curvature; the energies $\overline{A}\kappa^2$, $\overline{\mathcal{D}}\kappa$ and $\overline{\mathcal{K}}$ are shown in Fig. 3(b). Without SOC, we find that Eq. 2 exactly holds within numerical accuracy. This is not unexpected: in absence of SOC the energy no longer depends on the global quantization axis, but only on the relative angle between neighboring spins. This implies an exact degeneracy ($E_r = E_\varphi = E_{n=2} = \overline{A}\kappa^2$) between the “radial”, “azimuthal”, and $n = 2$ cycloidal

states on one hand, and between the “axial” and “perpendicular” states ($E_\zeta = E_\perp = 0$) on the other hand. These combined facts prove that the aforementioned violation [Fig. 3(a)] of Eq. (2) is entirely due to SOC.

The above analysis reveals an impact of relativistic effects on the curvilinear spin Hamiltonian, far more profound than previously believed. Existing models [14–16] limit their account of relativistic effects to including a curvature-independent anisotropy constant K_0 , while any impact of SOC on effective anisotropy and DMI interactions is systematically neglected. Our results show that such an assumption is reasonable in the case of the effective DMI, whose deviations from the predictions of Eq. 2 are of the order of 20%. The two anisotropy constants \mathcal{K}_φ and \mathcal{K}_r , however, display a very different curvature dependence in presence of SOC, in stark disagreement with the non-relativistic relationships of Eq. 2. Remarkably, our calculated \mathcal{K}_φ is *opposite in sign* to what would result from the physics of isotropic exchange alone. This shows that SOC needs to be taken into account in the calculation of the effective anisotropy of bent layers, as its neglect might lead to qualitatively wrong physical answers. For a quantitative comparison, in Table I we list the lowest-order fitted coefficients of $A(\kappa)$, $\mathcal{K}_\alpha(\kappa)$ and $\mathcal{D}(\kappa)$, with and without SOC. Clearly, the spin stiffness (A_0 and A_2) is not substantially affected by SOC. Also the effective DMI, $\overline{\mathcal{D}}_1 = 2\overline{A}_0 = 85.8$ meVÅ²/Cr is comparable to $\mathcal{D}_1 = 67.6$ meVÅ²/Cr with SOC. The leading order change in \mathcal{K}_φ , would correspond to $\overline{A}_0 = 42.9$ meVÅ²/Cr in the view of earlier models, in clear contrast to the value of -76.9 meVÅ²/Cr found from our DFT calculations including SOC.

Conclusions - We have used non-collinear magnetic DFT calculations, with and without SOC, to investigate the interplay of curvature and magnetism in monolayer CrI₃. Our calculations, in addition to a crossover between two spin states of distinct symmetry, have demonstrated that the effects of SOC are essential to take into account for a quantitatively (and sometimes even qualitatively) accurate description of the flexomagnetic coupling parameters. The obvious question is whether these conclusions are specific to the material considered here, or whether they are relevant to a broader range of systems. We can’t give a definite answer at this stage, but we can certainly speculate on how effective the present strategy may be in studying other cases. The main limitation we see in this context is related to computational power: While adapting our method to other 2D layers appears straightforward, the study of thicker membranes may be out of reach at present, due to the costly nanotube geometry. A way forward may be provided by the so-called cyclic DFT method, [49] which allows for calculating bent structures at a significantly lower computational cost; whether such an approach is effective in non-collinear spin structures, however, remains to be

Table I. Fitted leading order coefficients for the curvature dependence of spin stiffness, anisotropy and DMI, of the form: $A = A_0 + A_2\kappa^2$, $\mathcal{K}_r = -\mathcal{K}_0 + \mathcal{K}_{r,2}\kappa^2 + \mathcal{K}_{r,4}\kappa^4$, $\mathcal{K}_\varphi = \mathcal{K}_{\varphi,2}\kappa^2 + \mathcal{K}_{\varphi,4}\kappa^4$ and $\mathcal{D} = \mathcal{D}_1\kappa + \mathcal{D}_3\kappa^3$.

	A_0 (meVÅ ² /Cr)	A_2 (eVÅ ⁴ /Cr)	\mathcal{K}_0 (meV/Cr)	$\mathcal{K}_{r,2}$ (meVÅ ² /Cr)	$\mathcal{K}_{\varphi,2}$ (meVÅ ² /Cr)	\mathcal{D}_1 (meVÅ ² /Cr)
No SOC	42.9	5.7	0	55.1	55.1	101.2
With SOC	40.7	5.7	0.75	19.9	-76.9	67.6

seen. An alternative possibility would be treating curvature perturbatively via flexural phonons, in analogy to the ongoing efforts in the theory of flexoelectricity [50]; this could possibly allow one to work with the primitive cell of the flat crystal, with considerable savings in computer power. Exploration of these promising avenues, together with the discussion of other related physical effects going beyond the Hamiltonian of Eq. 1, will be an exciting topic for future studies.

Acknowledgments - We acknowledge financial support from the Swedish Research Council (VR - 2018-06807). M.S. acknowledges the support of Ministerio de Economía, Industria y Competitividad (MINECO-Spain) through Grants No. PID2019-108573GB-C22 and Severo Ochoa FUNFUTURE center of excellence (CEX2019-000917-S); of Generalitat de Catalunya (Grant No. 2017 SGR1506); and of the European Research Council (ERC) under the European Union's Horizon 2020 research and innovation program (Grant Agreement No. 724529). P.B. and S.P. acknowledge financial support from Italian MIUR under the PRIN project "Tuning and understanding Quantum phases in 2D materials - Quantum2D", grant n. 2017Z8TS5B and "TWEET: Towards Ferroelectricity in two dimensions", grant n. 2017YCTB59, respectively. D.A. and S.P. acknowledge financial support by the Nanoscience Foundries and Fine Analysis (NFFA-MIUR Italy) project. The authors thankfully acknowledge the computer resources at Pirineus and the technical support provided by CSUC (RES-FI-2021-1-0034). Additionally, computational work was done on resources at PDC, Stockholm via the Swedish National Infrastructure for Computing (SNIC).

- [1] P. Zubko, G. Catalan, and A. K. Tagantsev, *Annual Review of Materials Research* **43**, 387 (2013).
- [2] R. Streubel, P. Fischer, F. Kronast, V. P. Kravchuk, D. D. Sheka, Y. Gaididei, O. G. Schmidt, and D. Makarov, *Journal of Physics D: Applied Physics* **49**, 363001 (2016).
- [3] D. D. Sheka, *Applied Physics Letters* **118**, 230502 (2021).
- [4] H. Lu, C.-W. Bark, D. Esque de los Ojos, J. Alcala, C. B. Eom, G. Catalan, and A. Gruverman, *Science* **336**, 59 (2012).
- [5] U. K. Bhaskar, N. Banerjee, A. Abdollahi, Z. Wang, D. G. Schlom, G. Rijnders, and G. Catalan, *Nature Nanotechnology* **11**, 263 (2016).
- [6] L. Shu, S. Ke, L. Fei, W. Huang, Z. Wang, J. Gong, X. Jiang, L. Wang, F. Li, S. Lei, Z. Rao, Y. Zhou, R.-K. Zheng, X. Yao, Y. Wang, M. Stengel, and G. Catalan, *Nature Materials* **19**, 605 (2020).
- [7] A. Fasolino, J. H. Los, and M. I. Katsnelson, *Nature Materials* **6**, 858 (2007).
- [8] O. M. Volkov, A. Kákay, F. Kronast, I. Mönch, M.-A. Mawass, J. Fassbender, and D. Makarov, *Phys. Rev. Lett.* **123**, 077201 (2019).
- [9] R. Hertel, *SPIN* **03**, 1340009 (2013).
- [10] P. Gentile, M. Cuoco, and C. Ortix, *SPIN* **03**, 1340002 (2013).
- [11] P. Gentile, M. Cuoco, and C. Ortix, *Phys. Rev. Lett.* **115**, 256801 (2015).
- [12] A. Pyatakov, A. Sergeev, F. Mikailzade, and A. Zvezdin, *Journal of Magnetism and Magnetic Materials* **383**, 255 (2015), selected papers from the sixth Moscow International Symposium on Magnetism (MISM-2014).
- [13] J. A. Otálora, M. Yan, H. Schultheiss, R. Hertel, and A. Kákay, *Phys. Rev. Lett.* **117**, 227203 (2016).
- [14] O. V. Pylypovskiy, V. P. Kravchuk, D. D. Sheka, D. Makarov, O. G. Schmidt, and Y. Gaididei, *Phys. Rev. Lett.* **114**, 197204 (2015).
- [15] Y. Gaididei, V. P. Kravchuk, and D. D. Sheka, *Phys. Rev. Lett.* **112**, 257203 (2014).
- [16] D. D. Sheka, V. P. Kravchuk, and Y. Gaididei, *Journal of Physics A: Mathematical and Theoretical* **48**, 125202 (2015).
- [17] Y. Zhang, J. Liu, Y. Dong, S. Wu, J. Zhang, J. Wang, J. Lu, A. Rückriegel, H. Wang, R. Duine, H. Yu, Z. Luo, K. Shen, and J. Zhang, *Phys. Rev. Lett.* **127**, 117204 (2021).
- [18] A. Fernández-Pacheco, R. Streubel, O. Fruchart, R. Hertel, P. Fischer, and R. P. Cowburn, *Nature Communications* **8**, 15756 (2017).
- [19] C. Donnelly, M. Guizar-Sicairos, V. Scagnoli, S. Gliga, M. Holler, J. Raabe, and L. J. Heyderman, *Nature* **547**, 328 (2017).
- [20] M. Heide, G. Bihlmayer, and S. Blügel, *Physica B: Condensed Matter* **404**, 2678 (2009).
- [21] C. Xu, J. Feng, H. Xiang, and L. Bellaiche, *npj Computational Materials* **4**, 57 (2018).
- [22] D. Amoroso, P. Barone, and S. Picozzi, *Nature Communications* **11**, 5784 (2020).
- [23] S. Tiwari, M. L. Van de Put, B. Sorée, and W. G. Vandenberghe, *npj 2D Materials and Applications* **5**, 54 (2021).
- [24] B. Huang, G. Clark, E. Navarro-Moratalla, D. R. Klein, R. Cheng, K. L. Seyler, D. Zhong, E. Schmidgall, M. A. McGuire, D. H. Cobden, W. Yao, D. Xiao, P. Jarillo-Herrero, and X. Xu, *Nature* **546**, 270 (2017).
- [25] C. Gong, L. Li, Z. Li, H. Ji, A. Stern, Y. Xia, T. Cao, W. Bao, C. Wang, Y. Wang, Z. Q. Qiu, R. J. Cava, S. G. Louie, J. Xia, and X. Zhang, *Nature* **546**, 265 (2017).
- [26] M. A. McGuire, *Crystals* **7**, 121 (2017).

- [27] K. S. Burch, D. Mandrus, and J.-G. Park, *Nature* **563**, 47 (2018).
- [28] T. Song, X. Cai, M. W.-Y. Tu, X. Zhang, B. Huang, N. P. Wilson, K. L. Seyler, L. Zhu, T. Taniguchi, K. Watanabe, M. A. McGuire, D. H. Cobden, D. Xiao, W. Yao, and X. Xu, *Science* **360**, 1214 (2018).
- [29] M.-G. Han, J. A. Garlow, Y. Liu, H. Zhang, J. Li, D. DiMarzio, M. W. Knight, C. Petrovic, D. Jariwala, and Y. Zhu, *Nano Letters* **19**, 7859 (2019).
- [30] X. Yao, Y. Wang, and S. Dong, “Noncollinear topological textures in two-dimensional van der waals materials: From magnetic to polar systems,” (2021), [arXiv:2104.02208 \[cond-mat.mtrl-sci\]](https://arxiv.org/abs/2104.02208).
- [31] A. V. Kuklin, M. A. Visotin, W. Baek, and P. V. Avramov, *Physica E: Low-dimensional Systems and Nanostructures* **123**, 114205 (2020).
- [32] Y.-H. Shen, Y.-X. Song, W.-Y. Tong, X.-W. Shen, S.-j. Gong, and C.-G. Duan, *Advanced Theory and Simulations* **1**, 1800048 (2018).
- [33] W. Shi, Y. Guo, Z. Zhang, and W. Guo, *The Journal of Physical Chemistry C* **123**, 24988 (2019).
- [34] P. E. Blöchl, *Phys. Rev. B* **50**, 17953 (1994).
- [35] G. Kresse and D. Joubert, *Phys. Rev. B* **59**, 1758 (1999).
- [36] G. Kresse and J. Furthmüller, *Computational Materials Science* **6**, 15 (1996).
- [37] G. Kresse and J. Hafner, *Phys. Rev. B* **49**, 14251 (1994).
- [38] G. Kresse and J. Hafner, *Phys. Rev. B* **47**, 558 (1993).
- [39] S. L. Dudarev, G. A. Botton, S. Y. Savrasov, C. J. Humphreys, and A. P. Sutton, *Phys. Rev. B* **57**, 1505 (1998).
- [40] Using $8 \times 8 \times 1$ k -points changes the magnetic anisotropy of the monolayer by less than 3%.
- [41] M. Dresselhaus, G. Dresselhaus, and R. Saito, *Carbon* **33**, 883 (1995).
- [42] D. Hobbs, G. Kresse, and J. Hafner, *Phys. Rev. B* **62**, 11556 (2000).
- [43] P.-W. Ma and S. L. Dudarev, *Phys. Rev. B* **91**, 054420 (2015).
- [44] See Supplemental Material at [URL will be inserted by publisher] for a detailed discussion about fitting procedures for $A(1/R)$ and $\mathcal{D}(1/R)$, calculations without constraints on the spin directions, and comparison to other continuum models.
- [45] S. Kumar and P. Suryanarayana, *Nanotechnology* **31**, 43LT01 (2020).
- [46] Considering an area of $19.5 \text{ \AA}^2/\text{Cr}$.
- [47] S. I. Vishkayi, Z. Torbatian, A. Qaiumzadeh, and R. Asgari, *Phys. Rev. Materials* **4**, 094004 (2020).
- [48] Y. O. Kvashnin, A. Bergman, A. I. Lichtenstein, and M. I. Katsnelson, *Phys. Rev. B* **102**, 115162 (2020).
- [49] A. S. Banerjee and P. Suryanarayana, *Journal of the Mechanics and Physics of Solids* **96**, 605 (2016).
- [50] M. Stengel and D. Vanderbilt, “First-principles theory of flexoelectricity,” in *Flexoelectricity in Solids* (World Scientific Publishing Co.) Chap. Chapter 2, pp. 31–110.

Supplemental Material: Curved Magnetism in CrI₃

Alexander Edström

*Institut de Ciència de Materials de Barcelona (ICMAB-CSIC),
Campus UAB, 08193 Bellaterra, Spain and*

*Department of Applied Physics, School of Engineering Sciences,
KTH Royal Institute of Technology, AlbaNova University Center, 10691 Stockholm, Sweden*

Danila Amoroso and Silvia Picozzi

*Consiglio Nazionale delle Ricerche CNR-SPIN,
c/o Università degli Studi 'G. D'Annunzio', 66100, Chieti, Italy*

Paolo Barone

*Consiglio Nazionale delle Ricerche CNR-SPIN, Area della Ricerca di Tor Vergata,
Via del Fosso del Cavaliere 100, I-00133 Rome, Italy*

Massimiliano Stengel

*Institut de Ciència de Materials de Barcelona (ICMAB-CSIC),
Campus UAB, 08193 Bellaterra, Spain and*

ICREA - Institutió Catalana de Recerca i Estudis Avançats, 08010 Barcelona, Spain

This supplemental material contains a detailed description of the fitting procedure to obtain the parameters of the magnetic continuum model from the DFT data. Additionally, data from non-constrained, non-collinear magnetic DFT calculations are presented.

Fitting A , \mathcal{D} and \mathcal{K}

As introduced in the main text, we consider a continuum magnetic energy density

$$\varepsilon = A_\zeta [\partial_\zeta m_\alpha]^2 + A_\varphi [\partial_\varphi m_\alpha]^2 + \mathcal{K}_\varphi m_\varphi^2 + \mathcal{K}_r m_r^2 + \mathcal{K}_\zeta m_\zeta^2 + \mathcal{D} [m_r \partial_\varphi m_\varphi - m_\varphi \partial_\varphi m_r]. \quad (1)$$

Additional DM terms are allowed, but not relevant for the magnetic states considered here. We define $\mathcal{K}_\zeta = 0$. Further, we only consider states where $\partial_\zeta \mathbf{m} = 0$, whereby the first term vanishes and we call $A_\varphi = A$. α runs over the curvilinear coordinates and is summed over. The total magnetic energy is

$$E = \int_S \varepsilon[\mathbf{m}(\varphi, \zeta)] dS, \quad (2)$$

with integration over the surface S .

The value A_0 , of A in the zero curvature limit, can be determined from spin spiral calculations in a flat monolayer. The total energy as function of the propagation vector q is shown, with and without spin-orbit coupling (SOC), in Fig. 1, together with fits of the form $E = -\frac{\mathcal{K}_0}{2} + A_0 q^2$ with SOC and $E = \bar{A}_0 q^2$ without SOC, leading to the values $A_0 = 40.7 \text{ meV}\text{\AA}^2/\text{Cr}$ and $\bar{A}_0 = 42.9 \text{ meV}\text{\AA}^2/\text{Cr}$.

Considering a nanotube with circumference $L = 2\pi R$, and the radial magnetization state being analogous to the out-of-plane ferromagnetic state (the ground state) of a flat monolayer, then a magnetization $\mathbf{m} = \cos(n\varphi)\hat{r} - \sin(n\varphi)\hat{\varphi}$ corresponds to cycloidal spin spiral states with wavevector $q = \frac{2\pi n}{L} = \frac{n}{R} = n\kappa$. We calculated DFT total energies of these states for $0 \leq n \leq 4$, as illustrated in Fig. 2. For non-zero, integer values of n , the energy is

$$\varepsilon_n = An^2 - \mathcal{D}n + \frac{1}{2}(\mathcal{K}_\varphi + \mathcal{K}_r). \quad (3)$$

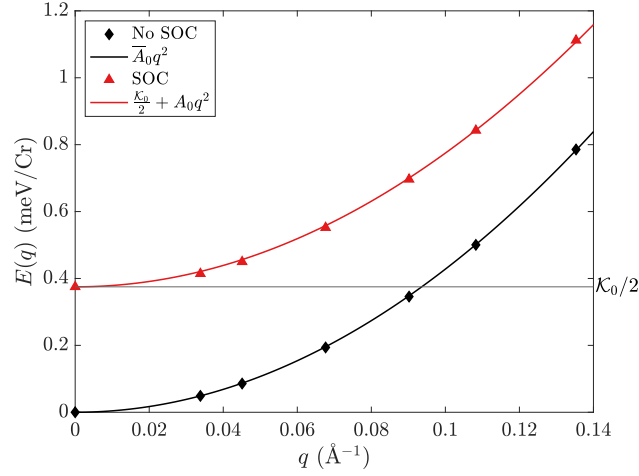


FIG. 1. Energy as function of propagation vector q for cycloidal spin spirals of the form $\mathbf{m}_i = [0, \sin(qy_i), \cos(qy_i)]$, in a flat monolayer.

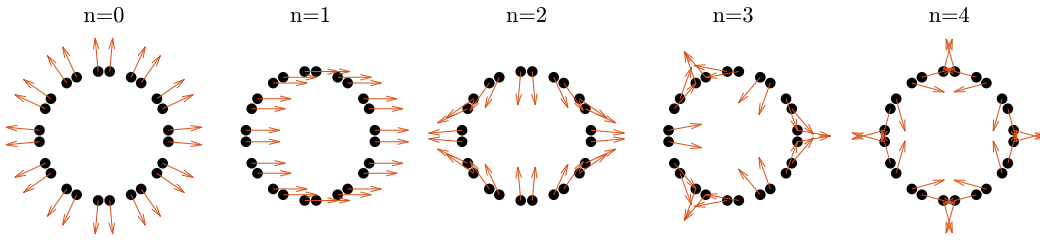


FIG. 2. Illustration of the nanotube cycloidal spin spiral states characterized by $n = qR$, for the $N = 6$ nanotube. Dots indicate Cr atoms and arrows their spins. Note that $n = 0$ corresponds to the radial magnetization state, and $n = 1$ to the state magnetized perpendicular to the tube axis.

For $n = 0$, which is the radial magnetization state, with SOC there is an extra contribution $(\mathcal{K}_r - \mathcal{K}_\varphi)/2$. Note that the linear dependence on n from the effective DMI term is a magnetochiral effect, whereby the energy depends on the direction of rotation of the spins. Fitting DFT calculated energies as function of n thus allows A , \mathcal{D} , \mathcal{K}_r and \mathcal{K}_φ to be evaluated. However, \mathcal{K}_r and \mathcal{K}_φ are already known from the data in Fig. 2 in the main text, leaving only A and \mathcal{D} to be determined. In the case with SOC, the energy of the axial magnetization state is additionally needed to define the zero energy.

The fittings of $E(n, N) = E(q, R)$ used to determine A and \mathcal{D} are plotted in Fig. 3. For small radii (N) and large wavevectors ($q \propto n$) the continuum approximation loses its validity. Thus, the fitting is only done using $n \leq 2$. For large N the fitted curves still agree well with the data points at $n = 3$, while there is an increasing discrepancy for decreasing N , as the continuum approximations breaks down. The same trend is seen at $n = 4$, but with an increased discrepancy between fitted curves and calculated points, compared to $n = 3$.

In the case without SOC, the spin states corresponding to $n = 0$ and $n = 2$ are degenerate. This is because these states have the same magnitude of the angles between neighboring spins. However, including SOC breaks this degeneracy by introducing magnetic anisotropy.

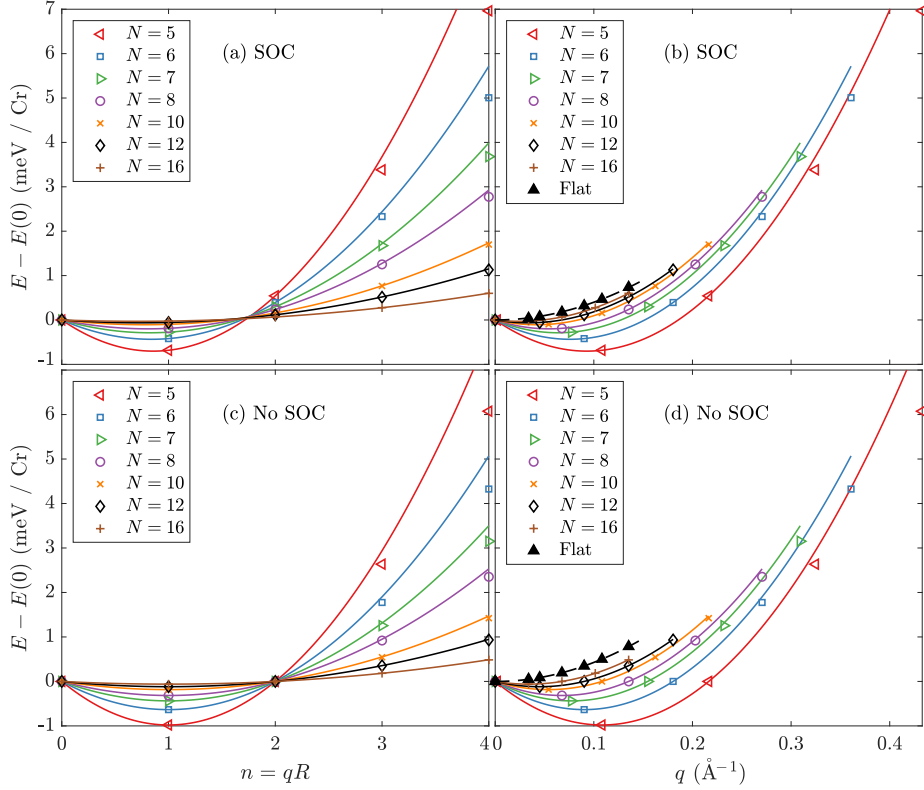


FIG. 3. Energy as function of $n = qR$ in (a) and (c) and of q in (b) and (d), for different nanotube radii $R = NR_0$, also showing quadratic fits for $0 \leq n \leq 2$ with solid lines. Data with SOC is shown in (a)-(b), and without SOC in (c)-(d). The data with SOC have been shifted by $E(0) = -\mathcal{K}_r/2$, known from Fig. 2 in the main text.

The fitted values for the spin stiffness A and DMI parameter \mathcal{D} , with and without SOC, are plotted as functions of curvature in Fig. 4. The fitted values for the anisotropy constants are plotted in Fig. 2 and Fig. 3 of the main text. By symmetry, the spin stiffness and anisotropy are even functions of curvature, while the effective DMI is odd. Consequently, they all contribute to the total energy as even functions of curvature (DMI contributes to the energy as $\mathcal{D}\kappa$). As discussed in the main text, and seen in Fig. 4, A is barely affected by SOC, while also the DMI behaves similarly with or without SOC. $A(\kappa)$ and $\mathcal{D}(\kappa)$ are fitted with 2nd and 3rd order polynomials respectively, so as to include energy contributions up to 4th order for all terms.

Based on Eq. 1, the relevant energies which have been calculated with DFT, considered in the main text, are $\varepsilon_r = \varepsilon_{n=0} = \mathcal{K}_r$, $\varepsilon_\varphi = \mathcal{K}_\varphi$, $\varepsilon_z = \mathcal{K}_z = 0$ and

$$\varepsilon_\perp = \varepsilon_{n=1} = \kappa^2 A - \kappa \mathcal{D} + \frac{1}{2}(\mathcal{K}_\varphi + \mathcal{K}_r). \quad (4)$$

Using the κ -dependence of A and \mathcal{D} shown in Fig 4, and the fittings for \mathcal{K}_r and \mathcal{K}_φ , the solid lines in Fig. 2 of the main text are drawn.

Without SOC, the energy is determined by the isotropic exchange term, which in the continuum/long wavelength limit is $\varepsilon_{\text{ex}} = A [\nabla \mathbf{m}]^2$. In the curvilinear coordinates ζ, φ, r , for a cylinder

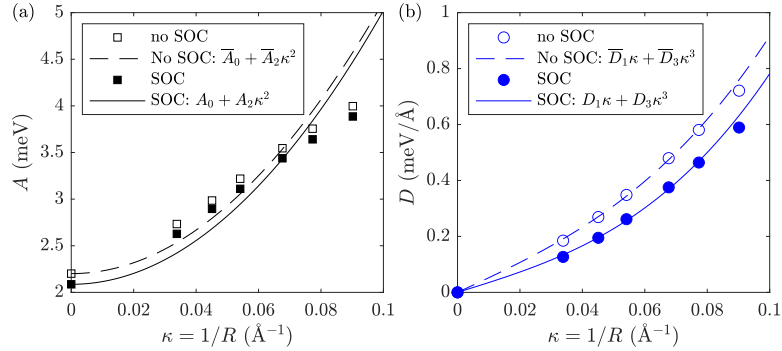


FIG. 4. (a) Spin stiffness $A(\kappa)$ and (b) DMI $\mathcal{D}(\kappa)$ as functions of curvature, with and without SOC. Lines show polynomial fits.

with radius R ,

$$\varepsilon_{\text{ex}} = \varepsilon_{\text{ex}}^{\text{eff}} + \overline{A}R^2 [m_r^2 + m_\varphi^2] + \frac{2\overline{A}}{R} [m_r \partial_\varphi m_\varphi - m_\varphi \partial_\varphi m_r] \quad (5)$$

$$= \varepsilon_{\text{ex}}^{\text{eff}} + \underbrace{\overline{\mathcal{K}} [m_r^2 + m_\varphi^2]}_{\varepsilon_{\text{ani}}^{\text{eff}}} + \underbrace{\overline{\mathcal{D}} [m_r \partial_\varphi m_\varphi - m_\varphi \partial_\varphi m_r]}_{\varepsilon_{\text{DMI}}^{\text{eff}}}, \quad (6)$$

with effective exchange, anisotropy and Dzyaloshinskii–Moriya interaction (DMI) terms. Accordingly, the curvature induced, non-relativistic, anisotropy and DMI constants are $\overline{\mathcal{K}} = \frac{\overline{A}}{R^2}$ and $\overline{\mathcal{D}} = \frac{2\overline{A}}{R}$, respectively. Note that $\overline{A} = \overline{A}(\kappa = 1/R)$ is also curvature dependent. As seen in Fig. 3 of the main text, the relations $\overline{\mathcal{K}} = \frac{\overline{A}}{R^2}$ and $\overline{\mathcal{D}} = \frac{2\overline{A}}{R}$ are very well fulfilled by the fitted values for \overline{A} , \mathcal{D} and \mathcal{K} .

Non-Constrained Magnetic Calculations

The DFT calculations discussed in the main text were performed using a constraint of $\Lambda = 5$ eV to keep the Cr spins in the directions defining each magnetic state considered. To check that the results are not significantly influenced by the constraint, we did some of the calculations also with $\Lambda = 10$ eV, confirming a negligible change to the energies. Next, we also performed calculations without constraints, but initializing the calculations into each of the magnetic states considered and allowing them to relax into near lying (meta-)stable states. The resulting states typically include small tilts of the spins away from the higher symmetry, ideal states considered in the constrained calculations. These small tilts are expected to occur due to microscopic spin interactions, beyond the continuum approximation, and will be further investigated in a future work. As seen in Fig. 5, the changes in the relevant energy differences, when comparing constrained and unconstrained calculations, are minute at small curvatures. This corroborates that the fitting of the continuum model at small curvatures is not affected by the constraint, which however, improves the numerical convergence of the calculations and allow well defined states to be compared at each curvature considered. At larger curvatures, for some states the non-constrained calculations may not converge at all, or into states that distinctly differ from the initial states, whereby a useful comparison cannot be to made.

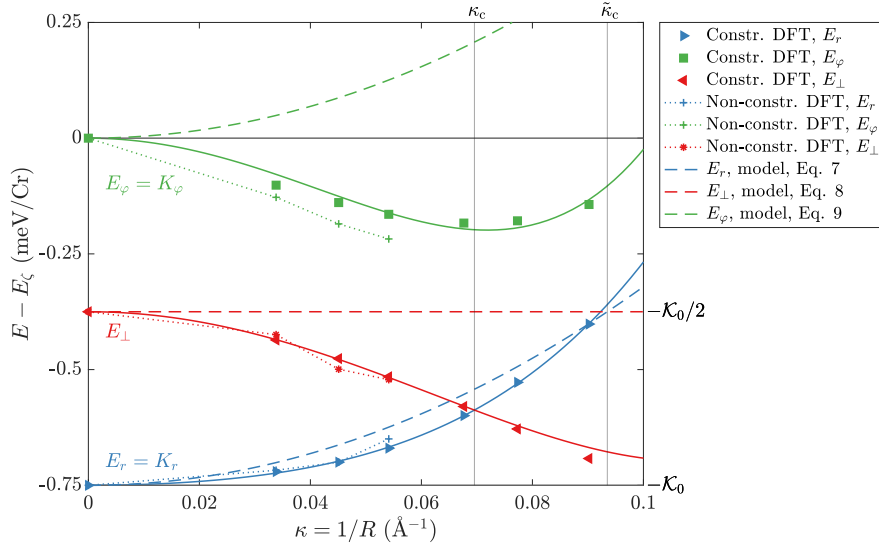


FIG. 5. Energies of magnetic states, relative to E_ζ , as function of curvature in CrI_3 nanotubes, using constrained or non-constrained, non-collinear magnetic DFT calculations, with SOC. Additionally, the energies predicted by the model in Eq. 7 are shown as dashed lines.

Comparison to Continuum Models

Earlier work based on phenomenological continuum models [1–4] described curvilinear magnetism in 1D and 2D using a model considering two terms: one for the isotropic exchange stiffness and one anisotropy term. The energy in the 2D case is

$$E = \int [A(\nabla \mathbf{m})^2 - K_0(\hat{\mathbf{m}} \cdot \hat{\mathbf{n}})^2] dS, \quad (7)$$

with magnetization density \mathbf{m} , integration over the surface S with normal $\hat{\mathbf{n}}$, and curvature-independent spin stiffness A and anisotropy constant K_0 . In this model, the effect of spin-orbit coupling is incorporated in the magnetic anisotropy of the second term. Based on Eq. 7, the energy densities (per surface area) of the three magnetic states, discussed in the main text, are

$$E_r = -K_0 + A\kappa^2 \quad (8)$$

$$E_\perp = -K_0/2 \quad (9)$$

$$E_\varphi = A\kappa^2. \quad (10)$$

Using the calculated values for CrI_3 , $A = \bar{A}_0 = 42.9$ ($\text{meV}\text{\AA}^2/\text{Cr}$) and $K_0 = 0.75$ meV/Cr , in Eq. 8-10, leads to the dashed curves in Fig. 5. Comparing these to the DFT results reveals clear qualitative and quantitative differences. For E_φ , Eq. 7 predicts an increase in energy with curvature, relative to the axial magnetization, whereas the DFT calculations show that E_φ decreases. In a material with negative K_0 , favoring in-surface magnetization, this would lead to different predictions for the magnetic ground state of the curved material.

Also in the case of E_\perp the qualitatively different behavior is clear; while Eq. 9 predicts a curvature-independent value, the DFT calculations reveal that E_\perp decreases with increasing curvature.

In the case of E_r , the model results and the DFT data agree that the energy increases with curvature. However, the leading order (quadratic) coefficient is sharply different, with the one for the dashed line being $\bar{A}_0 = 42.9 \text{ meV}\text{\AA}^2/\text{Cr}$, and that of the solid line $K_{r,2} = 19.9 \text{ meV}\text{\AA}^2/\text{Cr}$.

Regardless the qualitative differences in the predictions of Eq. 7 and the DFT data, the crossover from the radial to the perpendicular magnetization state is achieved in both cases (the red and blue lines cross each other both, for the dashed and solid lines), although at different curvatures; the crossover is found to be $\kappa = 0.070 \text{ \AA}$ from the DFT calculations and $\kappa = 0.094 \text{ \AA}$ in the model of Eq. 7. This implies that the essential physics to describe the magnetic crossover is the competition between the usual magnetic anisotropy, occurring already without curvature due to SOC, and effective anisotropy or DMI terms emerging from the isotropic exchange interaction, as a result of curvature. Nevertheless, the complete first principles treatment, including SOC, leads to important alterations to the curvature dependence of the relevant terms in the magnetic energy, that may lead to distinctly different magnetic ground states in other materials.

-
- [1] Y. Gaididei, V. P. Kravchuk, and D. D. Sheka, *Phys. Rev. Lett.* **112**, 257203 (2014).
 - [2] O. V. Pylypovskyi, V. P. Kravchuk, D. D. Sheka, D. Makarov, O. G. Schmidt, and Y. Gaididei, *Phys. Rev. Lett.* **114**, 197204 (2015).
 - [3] D. D. Sheka, V. P. Kravchuk, and Y. Gaididei, *Journal of Physics A: Mathematical and Theoretical* **48**, 125202 (2015).
 - [4] R. Streubel, P. Fischer, F. Kronast, V. P. Kravchuk, D. D. Sheka, Y. Gaididei, O. G. Schmidt, and D. Makarov, *Journal of Physics D: Applied Physics* **49**, 363001 (2016).